



Characteristics of SEN clogging and adhesive behavior of oxide inclusion during continuous casting of Ti-stabilized ultra-pure ferritic stainless steels

Xue-feng Bai¹ · Yan-hui Sun¹ · Hui-bin Wu¹

Received: 13 July 2022 / Revised: 16 September 2022 / Accepted: 19 September 2022 / Published online: 3 November 2022
© China Iron and Steel Research Institute Group 2022

Abstract

Submerged entry nozzle (SEN) clogging during continuous casting of Ti-stabilized ultra-pure ferritic stainless (Ti-UPFS) steels was systematically investigated via cross-sectional analysis and acid dissolution treatment. The SEN deposit profile was characterized as occurring in three major layers: (1) an eroded refractory layer; (2) an initial adhesive layer comprised an $\text{Al}_2\text{O}_3\text{-ZrO}_2$ composite sub-layer and a dense Al_2O_3 -based deposit sub-layer; and (3) a porous multiphase deposit layer mainly consisting of $\text{MgO}\cdot\text{Al}_2\text{O}_3$, $\text{CaO}\text{-Al}_2\text{O}_3$, and $\text{CaO}\text{-TiO}_x$. The $\text{MgO}\cdot\text{Al}_2\text{O}_3$ -rich inclusions did not adhere directly to the eroded refractory but were entrapped during the deposit growth. Results of inclusion characterization in the tundish revealed that the $\text{MgO}\cdot\text{Al}_2\text{O}_3$ -rich particles present in the tundish served as the primary source of clogging deposits. Furthermore, a novel cavity-induced adhesion model by circular approximation was established to explain the effects of complex inclusion characteristics and refractory material type on adhesion force. A high number of small $\text{MgO}\cdot\text{Al}_2\text{O}_3$ inclusions were expected to accelerate the buildup of clogging deposits. Improving the modification of $\text{MgO}\cdot\text{Al}_2\text{O}_3$ -rich inclusions in the size range of 2–4 μm by Ca treatment was crucial to minimizing the risk of SEN clogging during the continuous casting of Ti-UPFS steels.

Keywords Ti-stabilized ultra-pure ferritic stainless steel · Submerged entry nozzle clogging · $\text{MgO}\cdot\text{Al}_2\text{O}_3$ -rich inclusion · Adhesion · Continuous casting

1 Introduction

Ti-stabilized ultra-pure ferritic stainless (Ti-UPFS) steels achieve excellent mechanical properties and corrosion resistance by reduction of C and N contents and addition of Ti as a stabilizer [1]. However, the presence of Ti enhances the clogging ability of the submerged entry nozzle (SEN), thereby severely impacting productivity during continuous casting and causing unacceptable product defects [2–4].

In Ti-free Al-killed steels, solid inclusions with a high melting temperature, including Al_2O_3 , $\text{MgO}\cdot\text{Al}_2\text{O}_3$, CaS, $\text{CaO}\cdot 6\text{Al}_2\text{O}_3$, and $\text{CaO}\cdot 2\text{Al}_2\text{O}_3$, can deteriorate castability [5–7]. These existing inclusions as products of deoxidation

and improper Ca modification are generally considered as the major origin of nozzle blockage build-ups [7]. In addition, a network of Al_2O_3 layer caused by the reaction between Al in molten steel and CO gas generated from the nozzle can initially form on the inner surface of the nozzle wall and accelerate the deposition of suspended inclusions [8].

Considering the strong affinity of Ti with O and N [9], the clogging behavior in Ti-bearing steels is considerably dissimilar to, and more serious than, that in Al-killed steels in the absence of Ti. Table 1 summarizes the published research on the characteristics and causes of SEN clogging in Al-killed Ti-bearing steel over the past two decades. In addition to the solid particles mentioned above, several Ti-bearing particles, such as TiN [4], TiO_x [10], $\text{Al}_2\text{O}_3\text{-TiO}_x$ [11, 12], and $\text{CaO}\text{-TiO}_x$ [13], are frequently observed in clogs depending on the refining and continuous casting techniques being used. In practice, deposits within a single nozzle can contain a combination of two or more types of

✉ Yan-hui Sun
sunyanhui@metall.ustb.edu.cn

¹ Collaborative Innovation Center of Steel Technology, University of Science and Technology Beijing, Beijing 100083, China

Table 1 Reported characteristics and causes of SEN clogging during continuous casting of Al-killed Ti-bearing steel in recent studies

Authors	Year	Steel	Nonmetallic phase in deposits	Main findings
Cheng et al. [14]	2021	Ca-treated Al-killed Ti-bearing steel	CaO–TiO _x , Al ₂ O ₃ –MgO and Al ₂ O ₃ –CaO–SiO ₂	A low-melting-point interaction layer, as a reaction product of adhered inclusions and refractory, penetrated into and damaged refractory material
Yan et al. [15]	2020	Ti-ULC steel (middle-thin billet process)	Al ₂ O ₃ and Al–Ti–O complex inclusion	A reaction layer resulting from reaction between oxidizing gas and Al and Ti in steel promoted inclusion deposition
Li et al. [16]	2019	AISI 441	(MgO–Al ₂ O ₃) _{rich} –CaO–TiO _x	Thermodynamics of various Ca contents and temperatures on inclusion chemistry in liquid steel
Dorrer et al. [17]	2019	Ti-ULC steel	Ti-bearing alumina	Ti-bearing alumina was formed after Fe–Ti-addition and accelerated buildup of clogging deposits
Lee et al. [18]	2019	Ti-ULC steel	Complicated oxide (CaO–Al ₂ O ₃ –TiO _x –...)	Increasing Al/Ti ratio lowered formation of FeO _r –Al ₂ O ₃ –TiO _x , reducing extent of nozzle clogging
Kang and Lee [12]	2019	Ti-ULC steel	Al ₂ O ₃ and FeO _r –Al ₂ O ₃ –TiO _x	Oxidation behavior of Al–Ti containing steel in tundish and in nozzle refractory
Sun et al. [4]	2016	AISI 321	TiN and MgO–Al ₂ O ₃ ; TiO ₂ transition layer	TiO ₂ layer resulting from an interfacial reaction between (SiO ₂) _{refractory} and [Ti] accelerated buildup of clogging deposits
Basu et al. [11]	2004	Ti-ULC steel	Al ₂ O ₃ , MgO–Al ₂ O ₃ and fine TiO _x –Al ₂ O ₃	TiO _x –Al ₂ O ₃ inclusions originated almost entirely due to reoxidation of molten steel during casting
Zheng et al. [19]	2006	AISI 409L	TiO ₂ and MgO–Al ₂ O ₃	Reoxidation of molten steel due to strong Ar stirring after Ti wire feeding increased amount of CaO·TiO ₂ –MgO·Al ₂ O ₃
Zhen et al. [20]	2005	AISI 321	CaO·TiO ₂ –MgO·Al ₂ O ₃	Reoxidation of molten steel during Ar stirring and casting increased amount of CaO·TiO ₂ –MgO·Al ₂ O ₃
Nunnington and Sutcliffe [3]	2001	AISI 321 and AISI 409	TiN and MgO–Al ₂ O ₃ in major clogs; TiO _x at interface	TiO _x was formed due to oxidation of TiN
Maddalena et al. [2]	2000	AISI 321 and AISI 409	Pure TiN and TiN connected via a MgO·Al ₂ O ₃	Presence of MgO·Al ₂ O ₃ accelerated growth rate of deposit

*Ti-ULC—Ti-ultra-low C steel

inclusions including complex inclusions, indicating that the deposits may have originated from different sources.

Through the protective casting and vacuum oxygen decarburization (VOD) refining technique [3, 4, 16], the TiN-type of SEN clogging caused by N pick-up in Ti-stabilized stainless steel has been significantly alleviated. However, the problem of SEN clogging caused by complex oxides in Ti-UPFS steels has not gone away. As listed in Table 1, a number of studies over the past two decades have provided important information in terms of the inclusion evolution in molten steel and deposit origination from thermodynamic considerations. With the aid of commercial thermodynamic software, like FactSage, the influences of steel chemistry on inclusions in the Cr-containing stainless steel system were estimated, which agreed well with the observed results [16]. Furthermore, some researchers have attempted to investigate the formation of the interaction layer and its contribution to nozzle clogging by considering wettability and heat transfer. In addition to

a network of Al₂O₃ mentioned above, a TiO₂ transition layer, which has a good wettability by Cr-containing stainless steel, can deteriorate the performance of castability by increasing the heat loss at the refractory–steel interface [3, 4, 19]. However, there has been little discussion about the relation between inclusion characteristics, adhesion of complex inclusions, and SEN clogging in Ti-UPFS steel.

The current analysis is developed from the perspectives of clog characterization and inclusion adhesion, providing a better understanding of the formation and mitigation of SEN clogging in Ti-UPFS steels. A comprehensive description of the characteristics of SEN deposits in Ti-UPFS steels was first provided via cross-sectional analysis and acid dissolution treatment. In addition, the adhesive behavior of existing complex inclusions at the refractory–steel interface was explained by establishing a novel cavity-induced adhesion model via circular approximation.

2 Experimental

2.1 Experimental procedure

The main production process flow of Ti-UPFS steels is as follows: Klöckner oxygen blowing maximillanshuetter converter → VOD → ladle furnace (LF) → billet continuous casting. During VOD refining, Al was added to the ladle at the initial stage of deoxidation. During the LF treatment, Ca treatment was performed prior to Ti alloying. The tundish was filled with 20-t liquid steel. It was equipped with a nozzle with inner diameter and length of 68 and 700 mm, respectively. The submerged depth was set to 140 mm. Tables 2 and 3 present the main chemical compositions of the steel and SEN refractory, respectively.

2.2 Characterization of deposits on nozzle wall

For the cross-sectional analysis, the deposits were collected and inlaid in petrographic specimens with epoxy glue. Then, the surface of the petrographic specimen was ground with SiC papers up to 1500 grit and subsequently polished with diamond paste. The composition and two-dimensional morphology of the deposits were obtained using a scanning electron microscope (SEM, Zeiss EVO 18 Special edition) combined with energy-dispersive X-ray spectroscopy (EDS, Bruker Nano XFlash detector 5010). The relative amounts of minerals in the deposits described by the area percentage were estimated using a metallographic microscope. A detailed description of mineralogical analysis can be found in the study conducted by Bai et al. [21].

Most of the inclusions in the deposits on the nozzle wall have various irregular shapes; thus, it is difficult to reveal the actual morphology by cross-sectional observations. Therefore, inclusions were extracted from the deposits for a three-dimensional analysis. Approximately 1 g of the deposit specimen was peeled from the nozzle wall. The specimen was dissolved in 100 mL hydrochloric acid solution (1:1 by volume) at 70 °C (Fig. 1). After the complete dissolution of the deposits, 150 mL distilled water was added to the solution, which was then reheated to 70 °C. Subsequently, the solution containing the inclusions was filtered using a polytetrafluoroethylene membrane with an open pore size of 0.2 μm. After filtration, the membrane was washed alternately six times with hot HCl

Table 3 Chemical composition of SEN refractory (wt.%)

Location	Al ₂ O ₃	SiO ₂	C	ZrO ₂
Bulk	45.65		21.28	
Slag line			12.45	75.68

(volume of 1:25) and hot distilled water to removal all iron salts. The membrane filter was mounted on an aluminum stub and coated with gold under vacuum conditions. The three-dimensional characteristics of the deposits were determined using a field emission SEM (Zeiss, Supra 55) combined with EDS (Oxford, INCA).

2.3 Characterization of existing non-metallic inclusions in tundish

A lollipop sample of liquid steel was taken from the tundish at the middle stage of casting. Subsequently, the sample was mounted and polished for inclusion analysis. The characteristics of inclusions were investigated using automated SEM–EDS analysis (Particle X, Thermo Fisher Scientific) with analyzed area of 55 mm². The working magnification was set to 400 × and the minimum detectable size of inclusions was 2.0 μm. The amount of inclusion can be described by the area fraction and number density.

3 Results and discussion

3.1 Characteristics of deposits on inner wall of SEN

Figure 2 shows a clog sample collected at the slag line of an SEN that was used for casting 480-t Ti-UPFS steel, covering a total casting time of 270 min. Based on the macroscopic and SEM–EDS analyses, the deposit profile on the nozzle wall could be characterized as occurring in three main layers: (1) an eroded refractory layer; (2) a grayish initial adhesive layer with thickness of 0.2–0.3 cm; and (3) a sepia porous multiphase deposit layer with thickness of 0.3–0.5 cm, which was covered by spherically solidified steel droplets.

Table 2 Chemical composition of stainless steel (wt.%)

C	Si	Mn	P	S	Cr	Ni	Ti	Nb	N	Fe
0.008	0.3	0.3	0.025	0.005	18.00	0.2	0.2	0.015	0.012	Balance

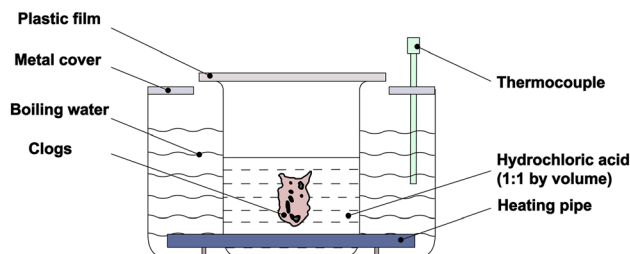


Fig. 1 Schematic of acid dissolution method

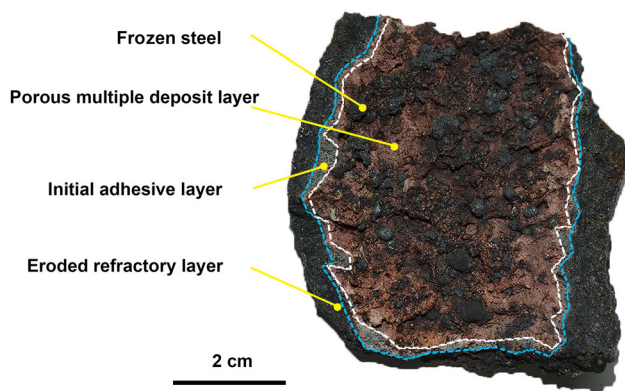


Fig. 2 Macroscopic features of SEN deposits

Figure 3 shows the distribution of the main elements at the interface between the initial adhesive and eroded refractory layers. Obviously, the surface layer of zirconia was damaged by steel erosion, resulting in steel infiltration into the refractory. It should be noted that a crucial layer, with thickness of approximately 0.2–0.3 cm and containing concentrated Al, Ca, Ti, and Zr was attached to the eroded wall. The appearance of this layer represents the growth of the deposits.

Figure 4 shows the distribution of the main elements in the initial adhesive layer. According to the EDS results, the initial adhesive layer further comprised two sub-layers: an

$\text{Al}_2\text{O}_3\text{-ZrO}_2$ composite layer, and a dense Al_2O_3 -based deposit layer. The $\text{Al}_2\text{O}_3\text{-ZrO}_2$ composite layer, which was closer to the refractory, occupies the right half of the mapping image, whereas the dense Al_2O_3 -based deposit layer on the side of the steel occupies the other side. The mapping results show no significant difference between the mapping patterns of the two sub-layers except for the Zr concentrated in the compact Al_2O_3 -based layer.

The fine details of the cross-sectional characteristics of the two Al_2O_3 -rich layers are shown in Fig. 5. Meanwhile, the mineral constitution of initial adhesive layer is listed in Table 4. The results show that the $\text{Al}_2\text{O}_3\text{-ZrO}_2$ composite layer mainly comprised Al_2O_3 , frozen steel, and ZrO_2 , whereas more CaO-TiO_x and less ZrO_2 were observed in the dense Al_2O_3 -based deposit layer. Additionally, there were significant differences between the morphology features and distributions of the Al_2O_3 phases of the two layers. In Fig. 5, the dark region in the $\text{Al}_2\text{O}_3\text{-ZrO}_2$ composite layer with a fibrous shape corresponded to the Al_2O_3 phase, which firmly adhered to the ZrO_2 . In contrast, the Al_2O_3 phase with an irregular polygonal shape in the dense Al_2O_3 -based deposit layer adhered to each other and formed a more compact structure than that in the $\text{Al}_2\text{O}_3\text{-ZrO}_2$ composite layer. Tehovnik et al. [22] reported that the Al_2O_3 that first adhered to the zirconia refractory was partially modified to $\text{CaO}\cdot 3\text{Al}_2\text{O}_3$ with CaSi . This differs from the findings of the present study.

The main element mapping results at the interface between the porous multiphase deposit and the dense Al_2O_3 -based deposit layers are shown in Fig. 6. The Mg-rich zone was located at the outermost layer with a distinct boundary line, whereas Ca and Al were distributed over nearly the entire scanning area. Despite the holes in the porous deposits, frozen steel was not observable in the porous multiphase deposits.

As shown in Fig. 7, the outermost layer of the deposits in contact with steel was mainly composed of porous multiphase deposits, including $\text{MgO-Al}_2\text{O}_3$, $\text{CaO-Al}_2\text{O}_3$,

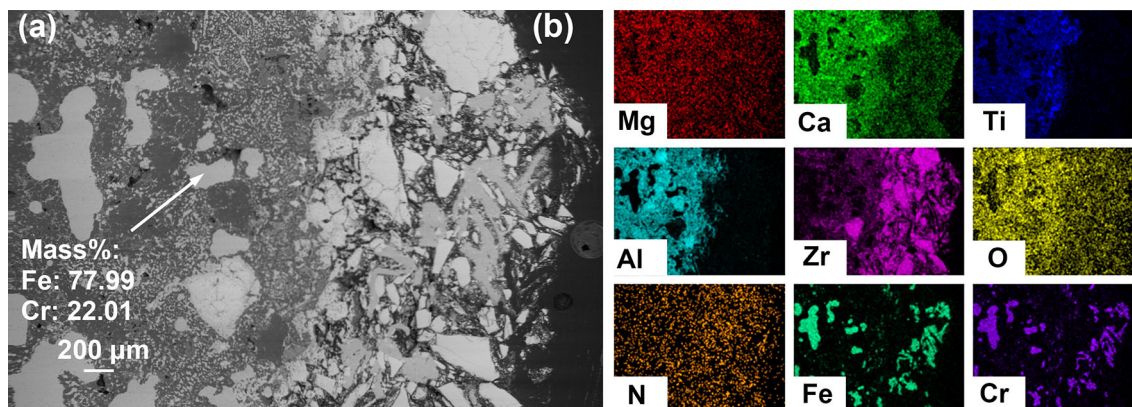


Fig. 3 Elemental distributions at interface between initial adhesive and eroded refractory layers. a Initial adhesive layer; b eroded SEN layer

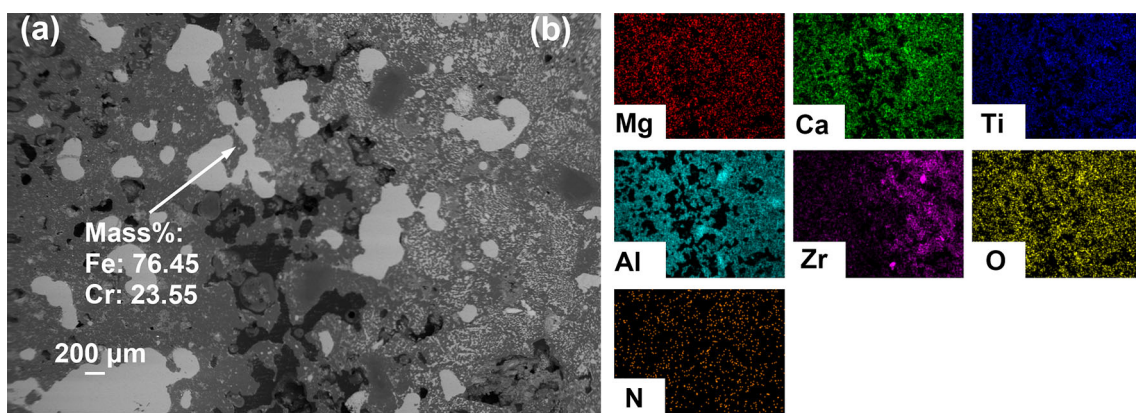


Fig. 4 Elemental distributions at interface between $\text{Al}_2\text{O}_3\text{-ZrO}_2$ composite and dense Al_2O_3 -based deposit layers. **a** Dense Al_2O_3 -based deposit layer; **b** $\text{Al}_2\text{O}_3\text{-ZrO}_2$ composite layer

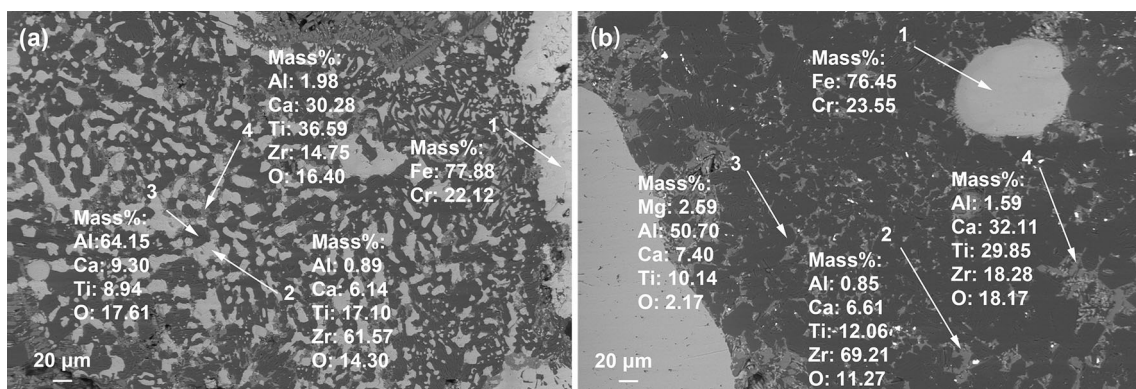


Fig. 5 Cross-sectional characteristics of deposits in initial adhesive layer. **a** $\text{Al}_2\text{O}_3\text{-ZrO}_2$ composite layer; **b** dense Al_2O_3 -based deposit layer

Table 4 Mineral constitution of initial adhesive layer

Layer	Area percentage/%			
	1-Steel	2-ZrO ₂	3-Al ₂ O ₃	4-CaO-TiO _x
$\text{Al}_2\text{O}_3\text{-ZrO}_2$ composite layer	15–20	20–25	40–45	5–10
Dense Al_2O_3 -based deposit layer	10–15	10–15	50–55	10–15

and CaO-TiO_x . The statistical results in Table 5 show that as the dominant phase in this layer, $\text{MgO}\cdot\text{Al}_2\text{O}_3$ accounted for 40%–45% of the total field of view. $\text{CaO}\cdot\text{Al}_2\text{O}_3$ with an irregular shape represented 30%–35% of the viewing field. In addition, a small amount of CaO-TiO_x was unevenly distributed between $\text{MgO}\cdot\text{Al}_2\text{O}_3$ and $\text{CaO}\cdot\text{Al}_2\text{O}_3$. Basu et al. [11] reported that $\text{Al}_2\text{O}_3\text{-TiO}_x$, the main Ti-bearing inclusion, was present at few locations in the clogged layer during the continuous casting of interstitial free (IF) steels. This discrepancy can be attributed to the inclusion modification by the Ca treatment.

Moreover, $\text{MgO}\cdot\text{Al}_2\text{O}_3$ and $\text{CaO}\cdot\text{Al}_2\text{O}_3$ were not detected in the eroded SEN and initial adhesive layers and their interface, which indicated that $\text{MgO}\cdot\text{Al}_2\text{O}_3$ and $\text{CaO}\cdot\text{Al}_2\text{O}_3$ did not adhere to the eroded refractory but grew on the existing dense Al_2O_3 -based deposits. A previous study suggested that $\text{MgO}\cdot\text{Al}_2\text{O}_3$ is entrapped in the outer clog layer that consists of porous alumina and steel during continuous casting of Ca-treated Al-killed steels [22].

Acid treatment allows for the direct analysis of the characteristics of the deposits. Considering the acid-resistances of inclusions and the refractory, and the compact structure of the initial adhesive layer, extracting particles directly from this layer is difficult. Figure 8 shows the three-dimensional morphologies of the $\text{MgO}\cdot\text{Al}_2\text{O}_3$ spinel inclusions in the porous multiphase deposit layer. As shown in Fig. 8a–c, single $\text{MgO}\cdot\text{Al}_2\text{O}_3$ octahedrons within a range of 2–10 μm directly adhered together and formed a large cluster. $\text{CaO}\cdot\text{TiO}_2$ associated with $\text{MgO}\cdot\text{Al}_2\text{O}_3$ could also be frequently observed on the membrane (Fig. 8d, e). As seen in Fig. 8f, the bridge is crucial in the adhesion of the existing inclusions that drives the SEN deposit growth. Nevertheless, no $\text{CaO}\cdot\text{Al}_2\text{O}_3$ deposits were observed in the

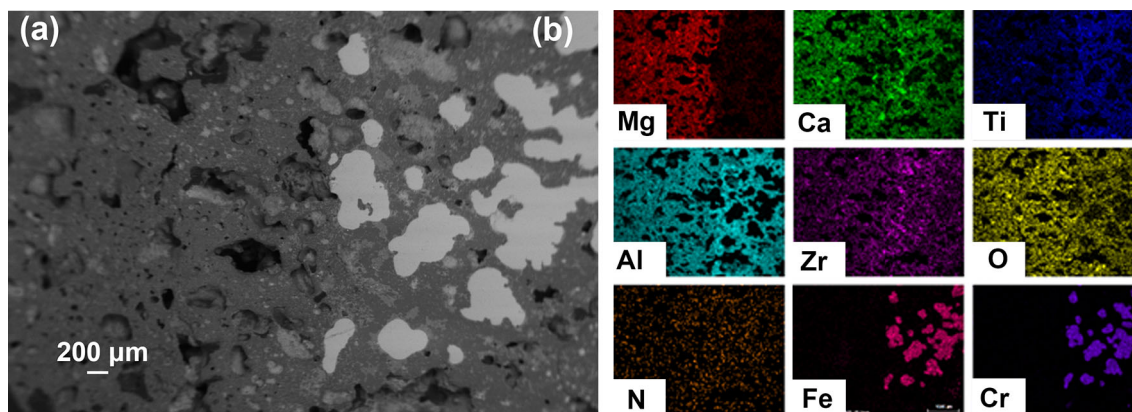


Fig. 6 Elemental distributions at interface between porous multiphase deposit and dense Al_2O_3 -based deposit layers. **a** Porous multiphase deposit layer; **b** dense Al_2O_3 -based deposit layer

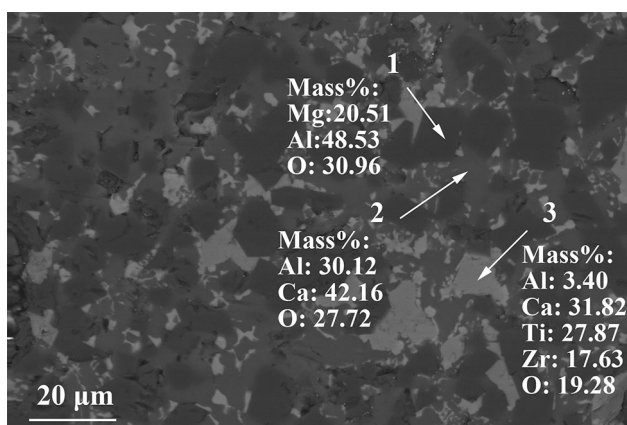


Fig. 7 Cross-sectional characteristics of deposits in porous multiphase deposit layer

Table 5 Mineral constitution of porous multiphase deposit layer

Phase	1-MgO- Al_2O_3	2-CaO- Al_2O_3	3-CaO- TiO_x
Area percentage/%	40–45	30–35	15–20

extraction results owing to the dissolution of $\text{CaO-Al}_2\text{O}_3$ deposits in the hydrochloric acid solution.

Figure 9 shows the morphologies of the other particles after the hot acid treatment. Figure 9a, b shows irregular polyhedral and coral-like CaO-TiO_x regularly occurring in the clogging deposit. Zirconia grains, with a smooth surface, sintered together and formed a cluster, as shown in Fig. 9c. In addition, a few small-sized TiN and TiO_xN_y particles were observed on the thin membrane.

3.2 Characteristics of inclusions in tundish

The amounts of various types of inclusions obtained by Particle X analysis are shown in Fig. 10. Considering the background effect of 20 wt.% Cr in steel matrix and smaller equilibrium content of chromium oxide [23], chromium oxide in the inclusions was not considered. Therefore, the inclusion classification rule for low-carbon Al-killed steels was adopted. Based on the statistical data, spinel-rich inclusions including pure spinel with a mean size of 3.7 μm , were the dominant inclusions in terms of both number density and area fraction. By comparison, even though no significant differences were observed between the most and second most abundant inclusion types in average size, the amount of alumina inclusion was far less than half of the amount of spinel-rich inclusion. In addition, a small number of small-sized TiN particles were frequently observed during automated SEM analysis.

The composition distribution of $\text{MgO-Al}_2\text{O}_3\text{-CaO-TiO}_x$ complex inclusions in the tundish is shown in Fig. 11. In this study, inclusion data with mass percentages of $(\text{MgO} + \text{Al}_2\text{O}_3 + \text{CaO})$, $(\text{MgO} + \text{Al}_2\text{O}_3 + \text{Ti}_3\text{O}_5)$, or $(\text{CaO} + \text{Al}_2\text{O}_3 + \text{Ti}_3\text{O}_5)$ larger than 90 wt.% were projected in the $\text{CaO-Al}_2\text{O}_3\text{-MgO-Ti}_3\text{O}_5$ pseudo-quaternary phase diagram. The dashed and dashed-dotted lines represent the 50 and 80 wt.% spinel phases in inclusions, respectively. Figure 11 shows that most of the inclusions were concentrated in the spinel-rich zone and Al_2O_3 corner. Furthermore, the size range of inclusions in the spinel-rich zone accords well with the three-dimensional observation results in Fig. 8, showing that the major source of SEN clogging was the exiting inclusion in the tundish. Furthermore, spinel content in inclusions decreased with

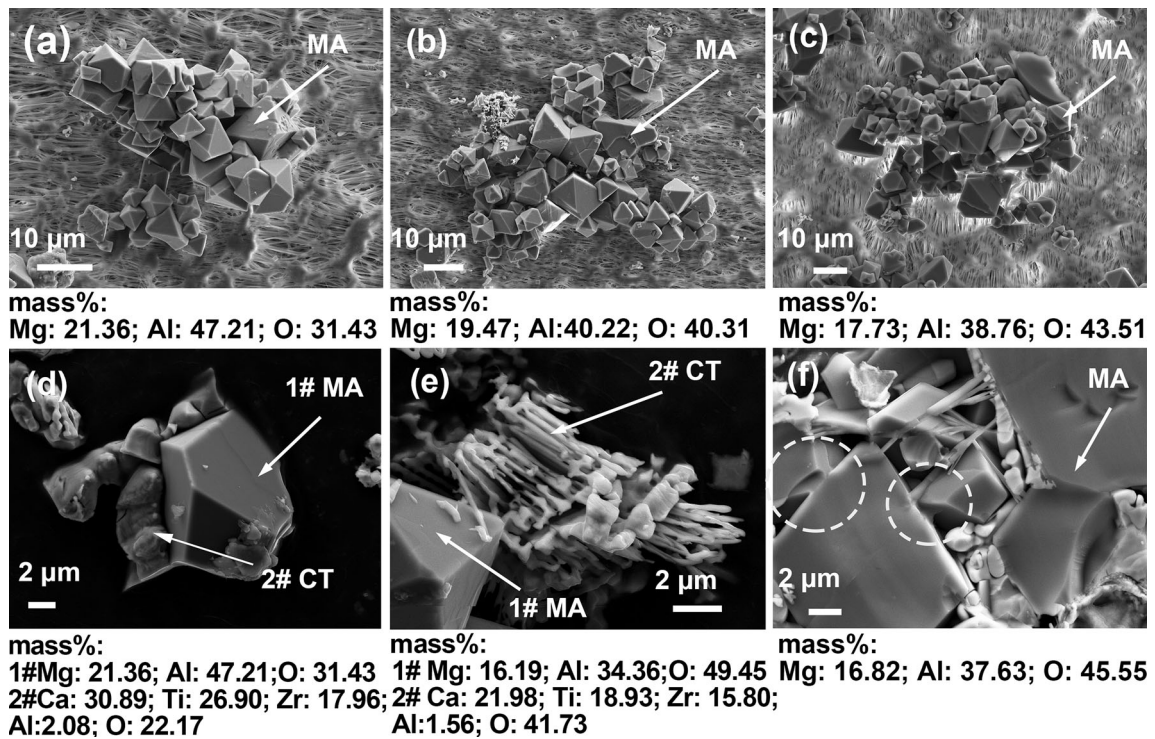


Fig. 8 Three-dimensional morphologies of $\text{MgO}\cdot\text{Al}_2\text{O}_3$ (MA) spinel inclusions in porous multiphase deposit layer. **a–c** $\text{MgO}\cdot\text{Al}_2\text{O}_3$ clusters; **d, e** $\text{MgO}\cdot\text{Al}_2\text{O}_3$ associated with $\text{CaO}\text{--}\text{TiO}_x$ (CT); **f** bridges between $\text{MgO}\cdot\text{Al}_2\text{O}_3$ spinel inclusions

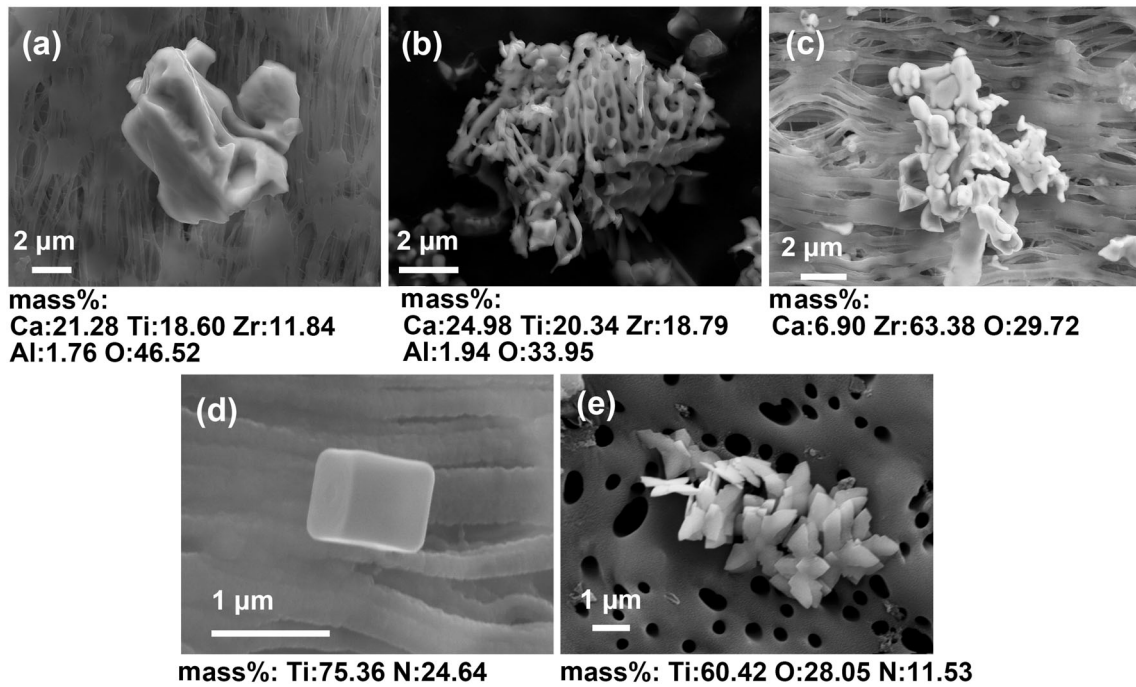


Fig. 9 Three-dimensional morphologies of other inclusions observed in deposits. **a, b** $\text{CaO}\cdot\text{TiO}_2$; **c** ZrO_2 ; **d** TiN ; **e** TiO_xN_y

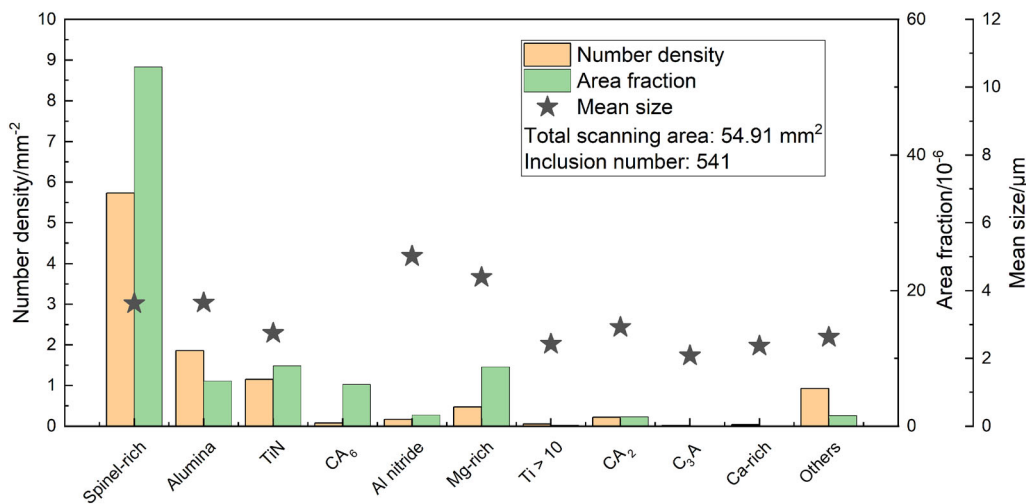


Fig. 10 Amounts of inclusion types in tundish. CA₆—CaO·6Al₂O₃; CA₂—CaO·2Al₂O₃; C₃A—3CaO·Al₂O₃

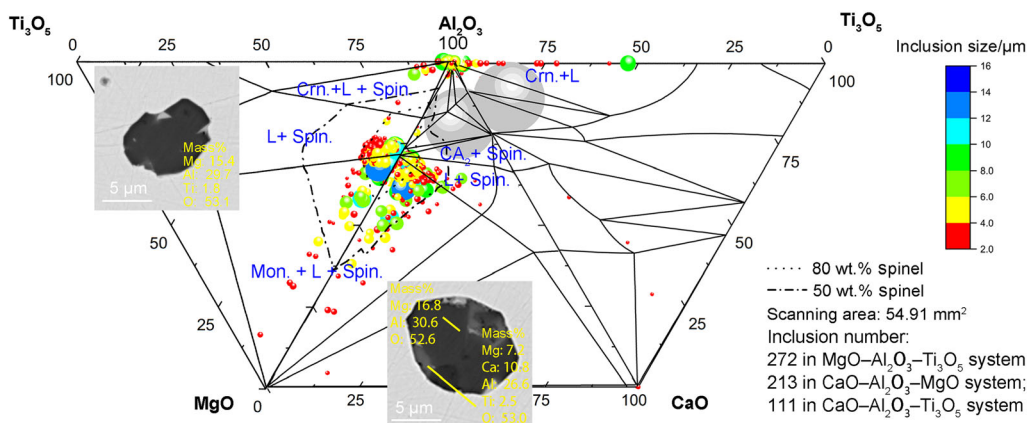


Fig. 11 Distribution of inclusion composition in tundish. L—Liquid oxide; Crn.—Corundum; Mon.—Monoxide; Spin.—Spinel

inclusion size. Note that spinel-rich particles exceeding 4 μm nearly fell within the 50 wt.% spinel regions of the pseudo-quaternary phase diagram. This is consistent with the conventional concept of their low modification effect by Ca treatment [24, 25]. Nevertheless, Kruger and Garbers-Craig [26], in a series of industrial-scale experiments, found that spinel inclusions exceeding 2 μm achieved complete modification after Ca addition in Ti-UPFS steels.

3.3 Adhesion of suspended inclusions

The profile of SEN deposits illustrates the vital role of the adhesion of suspended inclusions at the refractory–steel interface in the formation and growth of clogs. To explain their adhesive behaviors, a novel adhesion model is established with the following assumptions: (1) rigid

spherical inclusions are transported to the near-wall region by steel flow; (2) the nozzle wall and newly generated adhesive layer are assumed to be a smooth plane, meaning that the roughness caused by the erosion due to steel flow and the growth of clogs was not considered; (3) the temperature drop of the steel, chemical reactions, and phase transition during adhering are not considered; and (4) the meniscus of the cavity in the direction parallel to the axis of symmetry is simplified as a torus.

The adhesion force (F_A) resulting from the surface tension and the pressure difference between a cavity and molten steel can be described by Eq. (1) [27, 28]:

$$F_A = 2\pi\sigma R_N + \pi R_N^2 \Delta P, \tag{1}$$

where σ is the surface tension between molten steel, N m⁻¹; R_N is the neck and meniscus radii of the cavity, m; and ΔP is the pressure difference between a cavity and

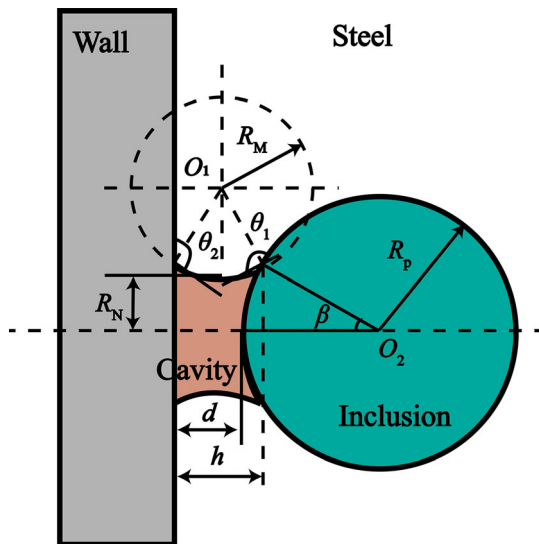


Fig. 12 Geometry of a cavity between a spherical particle and a plane at refractory–steel interface

molten steel, which is 1.8×10^5 Pa [29]. The relation between the neck and meniscus radii of a cavity is characterized by the Young–Laplace equation [30]:

$$\Delta P = \sigma \cdot \left(\frac{1}{R_M} - \frac{1}{R_N} \right), \tag{2}$$

where R_M is the meniscus radii of the cavity, m. Therefore, based on the geometry conditions shown in Fig. 12 and Young–Laplace relation, Eqs. (3)–(5) can be obtained:

$$h = R_p(1 - \cos \beta) + d, \tag{3}$$

$$h = R_M[-\cos(\theta_1 - \beta) - \cos \theta_2] \tag{4}$$

$$R_N = R_p \sin \beta - R_M[1 - \sin(\theta_1 - \beta)], \tag{5}$$

where R_p is the particle radius, m; θ_1 and θ_2 respectively denote the contact angles between inclusion and molten steel and between refractory and molten steel, ($^\circ$); β is the auxiliary angle introduced by the convergent point of phase

Table 6 Material properties used in calculation of adhesion force

Item	Contact angle of ceramic and molten steel/ $^\circ$	Density/ (kg m^{-3})	Surface tension/ (N m^{-1})
Al_2O_3	137 [31, 32]	3900 [33]	
ZrO_2	100 [28]		
$\text{MgO}\cdot\text{Al}_2\text{O}_3$	105 [34]	3580 [35]	
Liquid inclusion		2690 [36]	0.6 [37, 38]
Molten steel		6860 [39]	1.8 [40, 41]

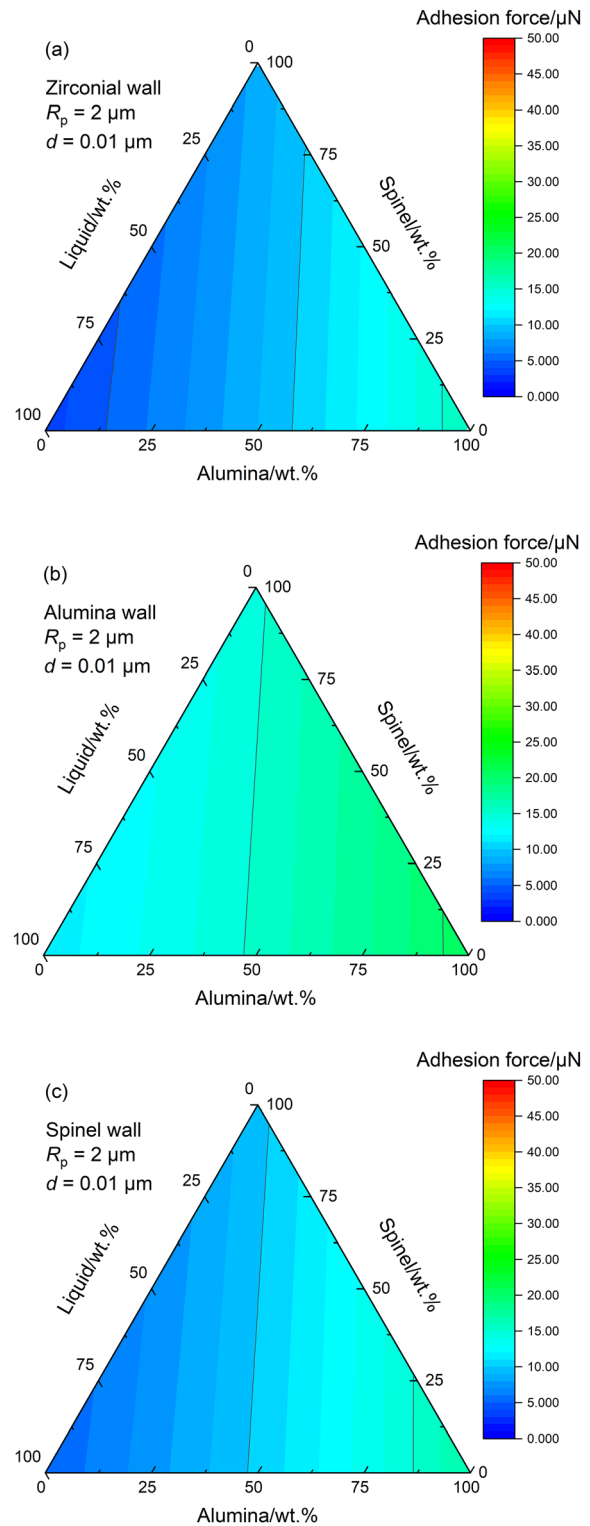


Fig. 13 Relation between inclusion chemistry, refractory material type, and adhesion force acting on a particle at refractory–steel interface. **a** Zirconia wall; **b** alumina wall; **c** spinel wall

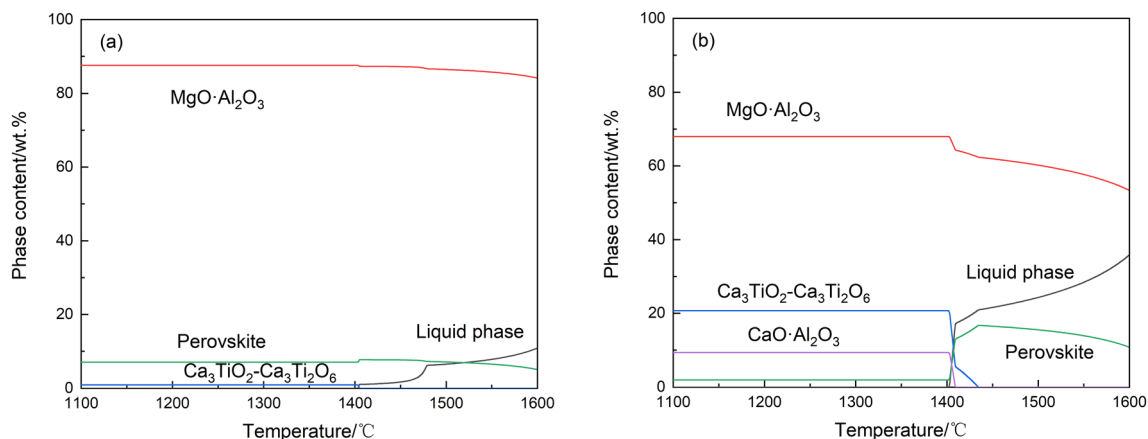


Fig. 14 Phase transformation of inclusions with decreasing temperature. **a** 4.45Ti₃O₅–5.11CaO–65.64Al₂O₃–24.80MgO with 10.86 wt.% liquid at 1600 °C; **b** 10.86Ti₃O₅–15.14CaO–54.74Al₂O₃–19.26MgO with 35.92 wt.% liquid at 1600 °C

boundaries, (°); d is the distance between the nozzle wall and surface of the particle, m; and h is the distance between the nozzle wall and the convergent point, m. Table 6 presents the values calculated for adhesion force.

Assuming that the molten steel and the liquid inclusion are in a completely wetted condition, the contact angle of the molten steel and the heterogeneous inclusion can be calculated according to Eq. (6) [42]:

$$\cos \theta = \sum_i f_i \cos \theta_i \quad (6)$$

where f_i is the fractional projected area of phase i in inclusion with the cavity neck surface, which is equal to the volume fraction of phase derived from inclusion chemistry; and θ_i is the contact angle of the molten steel and phase i , (°).

Figure 13 shows the calculated adhesion force acting on complex inclusions at the refractory–steel interface. The results show that the adhesion force acting on a heterogeneous inclusion could be weakened by increasing the liquid phase content. This means that the modification of a solid inclusion into a liquid inclusion or a small solid core covered by a liquid shell can alleviate the nozzle clogging. As shown in Fig. 13a, b, the increasing Al₂O₃ content significantly accelerated the adhesion forces acting on the particle at the surface of eroded refractory and initial adhesive layers. Hence, once the Al₂O₃-based inclusions were formed at the interface, the eroded refractory offered a favorable site for adhesion of the initial Al₂O₃-rich inclusions and the initial adhesive layer played a similar role in the formation of the porous clogging layer. In the case of the MgO·Al₂O₃ plate wall shown in Fig. 13c, the adhesion force slightly decreased compared with the results shown in Fig. 13b, but the force acting on a particle having large amount of high-melting-point phase was still high,

which therefore provided the driving force for the growth of the MgO·Al₂O₃-based porous layer.

Interestingly, despite of the intensive adhesion between Al₂O₃-based particles and MgO·Al₂O₃ spinel plate wall, the Al₂O₃ particles were hardly observed in the porous clogging layer. This indicates that the existing inclusion in the molten steel was not the sustainable source of the initial adhesive layer. The precipitation due to the decreasing oxygen solubility in high Cr melts with high dissolved oxygen content and reoxidation at the steel–refractory interface was most likely causes for the formation of the Al₂O₃ in the initial adhesive layer [18, 43].

Considering the temperature drop at the refractory–steel interface, the phase transformation occurred in the clogs at high temperature. However, prediction of chemistry evolution of each adhered inclusion is practically impossible in clogs because the adhesion of each complex inclusion cannot be ascertained a priori. Figure 14 predicts the phase transformation of two typical spinel-rich inclusions with various liquid contents during cooling by using the thermodynamic software FactSage 8.0. It can be seen that the content of MgO·Al₂O₃ was gradually increased with decreasing temperature. Besides, CaO–TiO_x and CaO–Al₂O₃ were more easily precipitated from the complex inclusion, which may be associated the results shown in Fig. 7.

The influence of inclusion size on the adhesion is shown in Fig. 15. Within the radius range shown in Fig. 15, the acceleration caused by the adhesion force decreased as the particle radius increased. Therefore, existing inclusions, which had a smaller size and more high-melting-point phase, tended to adhere to the inner wall of SEN once they were transported to the interface. Note that the dominant spinel-rich inclusions had a mean size of 3.7 μm in the tundish. Therefore, improving and achieving complete

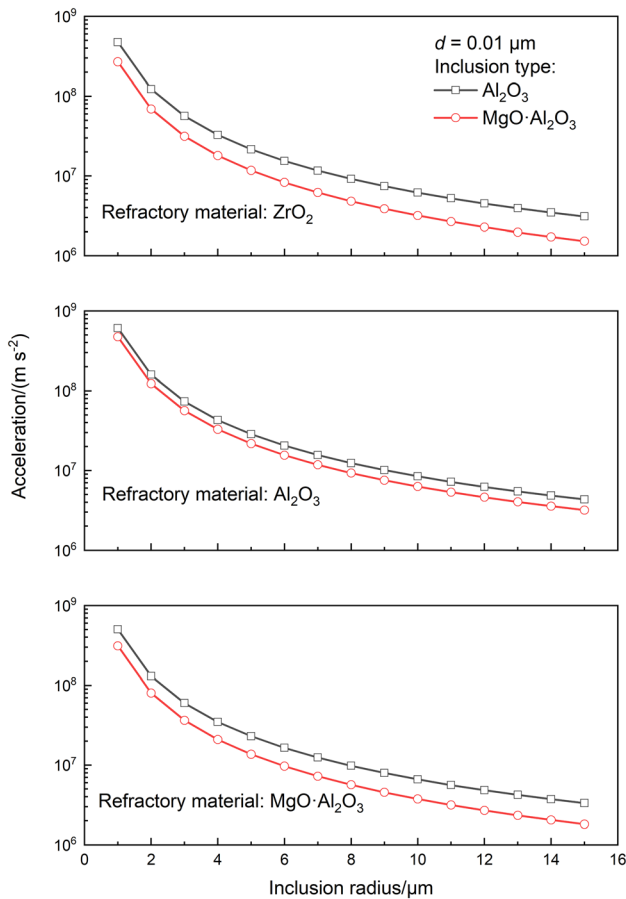


Fig. 15 Influence of particle size on acceleration due to adhesion

modification of spinel-rich inclusions in the size range of 2–4 μm by Ca treatment played a vital role in decreasing the tendency of SEN clogging during the casting of Ti-UPFS steels.

3.4 Mechanisms

The occurrence process of clogging is summarized in Fig. 16. When molten steel flowed through the nozzle, the erosion of the zirconia refractory by molten steel destroyed the protective layer on the surface of the nozzle base, thereby increasing the roughness of the inner nozzle wall as shown in Fig. 16a. Meanwhile, owing to the decreased solubility of oxygen in the steel and reoxidation at the refractory–steel interface, precipitated alumina inclusions and part of the molten steel were trapped in the damaged refractory material, thereby forming the initial adhesive layer (see Fig. 16b). The suspended particles that were not adequately modified by Ca treatment were transported toward the vicinity of the nozzle wall by turbulent flows [44] and subsequently adhered to the dense Al₂O₃-based deposit layer owing to the adhesion force. These particles were further sintered at the inner wall at high temperatures. Therefore, with the existing particles in the melt continuously sticking to the initial Al₂O₃-based layer and the newly generated porous multiphase deposit layer, clogs gradually grew on the inner wall of SEN during continuous casting (see Fig. 16c).

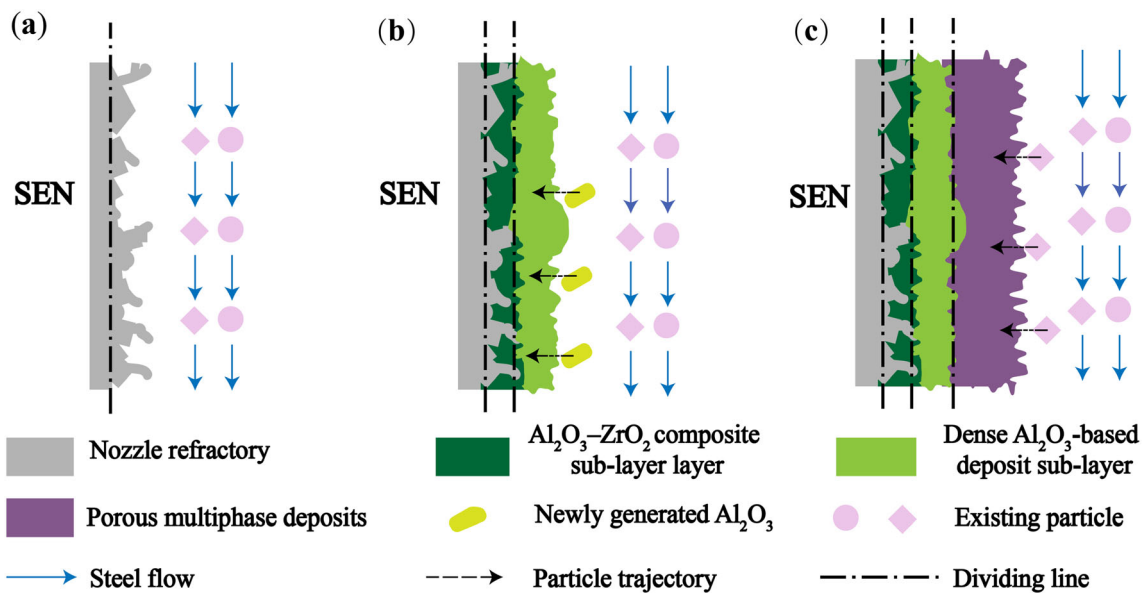


Fig. 16 Mechanism of SEN clogging in Ti-UPFS steels

4 Conclusions

1. The deposit profile on the nozzle wall could be divided into three main layers: eroded refractory layer, initial adhesive layer, and porous multiphase deposit layer. The initial adhesive layer was further composed of two sub-layers: an $\text{Al}_2\text{O}_3\text{-ZrO}_2$ composite layer and a dense Al_2O_3 -based deposit layer. The porous multiphase deposits mostly consisted of $\text{MgO}\cdot\text{Al}_2\text{O}_3$, $\text{CaO}\text{-Al}_2\text{O}_3$, and $\text{CaO}\text{-TiO}_x$.
2. The existing $\text{MgO}\cdot\text{Al}_2\text{O}_3$ -rich inclusions were entrapped during the deposit growth rather than adhering directly to the eroded refractory. The nozzle buildup in the porous multiphase deposit layer originated from the particles in the molten steel.
3. A novel cavity-induced adhesion model established by circular approximation was established. The adhesion behaviors of alumina and low modified spinel-rich particles were the direct causes of the formation of the initial adhesive layer and the growth of the porous multiphase deposit layer, respectively.
4. A high number of small sized $\text{MgO}\cdot\text{Al}_2\text{O}_3$ inclusions within steel caused a tendency towards SEN clogging. Practically, improving the modification of spinel-rich inclusions in the size range of 2–4 μm by Ca treatment played a crucial role in alleviating SEN clogging during continuous casting of Ti-UPFS steels.

Acknowledgements This work was financially supported by the National Natural Science Foundation of China (No. 51574026).

Declarations

Conflict of interest The authors declare no conflict of interest.

References

- [1] Y. Hou, G. Cheng, K. Kadoi, H. Inoue, Q.J. Ruan, J. Pan, X. Chen, *Metall. Mater. Trans. B* (2022) 2499–2511.
- [2] R. Maddalena, R. Rastogi, S. Bassem, A.W. Cramb, *Iron Steelmak. 27* (2000) 71–79.
- [3] R.C. Nunnington, N. Sutcliffe, in: 59th Electric Furnace Conference and 19th Process Technology Conference, Iron and Steel Society, Phoenix, USA, 2001, pp. 361–394.
- [4] Y. Sun, X. Bai, X. Yin, D. Duan, J. Jin, S. Fu, X. Zhu, *Chin. J. Eng.* 38 (2016) 109–118.
- [5] C. Hua, Y. Bao, M. Wang, *Powder Technol.* 393 (2021) 405–420.
- [6] Y.I. Ito, S. Nara, Y. Kato, M. Suda, *Tetsu-to-Hagané* 93 (2007) 355–361.
- [7] L. Zhang, B.G. Thomas, *Metall. Mater. Trans. B* 37 (2006) 733–761.
- [8] K. Sasai, Y. Mizukami, *ISIJ Int.* 34 (1994) 802–809.
- [9] X.R. Chen, G.G. Cheng, Y.Y. Hou, J.Y. Li, J.X. Pan, *J. Iron Steel Res. Int.* 27 (2020) 913–921.
- [10] Y. Gao, K. Sorimachi, *ISIJ Int.* 33 (1993) 291–297.
- [11] S. Basu, S.K. Choudhary, N.U. Girase, *ISIJ Int.* 44 (2004) 1653–1660.
- [12] Y.B. Kang, J.H. Lee, *Metall. Ital.* (2019) No. 1, 5–11.
- [13] H.G. Zheng, W.Q. Chen, *Steelmaking* 22 (2006) No. 3, 35–38.
- [14] L. Cheng, L. Zhang, Y. Ren, W. Yang, *Metall. Mater. Trans. B* 52 (2021) 1186–1193.
- [15] J. Yan, H.M. Yao, Z.G. Wu, Q.Y. Gao, *J. Iron Steel Res.* 32 (2020) 20–26.
- [16] J. Li, G. Cheng, Q. Ruan, J. Pan, X. Chen, *Metall. Mater. Trans. B* 50 (2019) 2769–2779.
- [17] P. Dorrer, S.K. Michellic, C. Bernhard, A. Penz, R. Rössler, *Steel Res. Int.* (2019) 1800635.
- [18] J.H. Lee, M.H. Kang, S.K. Kim, Y.B. Kang, *ISIJ Int.* 58 (2018) 1257–1266.
- [19] H. Zheng, B. Lu, S. Li, L. Wang, X. Chen, *Special Steel* 27 (2006) No. 6, 50–51.
- [20] H. Zhen, W. Chen, Q. Liu, P. Duan, L. Zhao, H. Wang, *J. Iron Steel Res.* (2005) No. 1, 14–18.
- [21] X. Bai, Y. Sun, L. Luo, C. Zhao, *J. Iron Steel Res. Int.* 27 (2020) 148–159.
- [22] F. Tehovnik, J. Burja, B. Arh, M. Knap, *Metalurgija* 54 (2015) 371–374.
- [23] X. Yin, Y. Sun, Y. Yang, X. Deng, M. Barati, A. McLean, *Ironmak. Steelmak.* 44 (2017) 152–158.
- [24] S. Yang, Q. Wang, L. Zhang, J. Li, K. Peaslee, *Metall. Mater. Trans. B* 43 (2012) 731–750.
- [25] C.B. Shi, W.T. Yu, H. Wang, J. Li, M. Jiang, *Metall. Mater. Trans. B* 48 (2017) 146–161.
- [26] D. Kruger, A. Garbers-Craig, *Metall. Mater. Trans. B* 48 (2017) 1514–1532.
- [27] R.A. Fisher, *J. Agric. Sci.* 16 (1926) 492–505.
- [28] U.D. Salgado, C. Weiß, S.K. Michellic, C. Bernhard, *Metall. Mater. Trans. B* 49 (2018) 1632–1643.
- [29] K. Sasai, Y. Mizukami, *ISIJ Int.* 41 (2001) 1331–1339.
- [30] A. Marmur, Tip-surface capillary interactions, *Langmuir* 9 (1993) 1922–1926.
- [31] K. Sasai, *ISIJ Int.* 54 (2014) 2780–2789.
- [32] L.C. Zhong, M. Zeze, K. Mukai, *Acta Metall. Sin. (Engl. Lett.)* 17 (2004) 795–804.
- [33] A. Murari, H. Albrecht, A. Barzon, S. Curiotto, L. Lotto, *Vacuum* 68 (2002) 321–328.
- [34] C.M. Fang, S.C. Parker, G. de With, *J. Am. Ceram. Soc.* 83 (2000) 2082–2084.
- [35] M.A.L. Braulio, M. Rigaud, A. Buhr, C. Parr, V.C. Pandolfelli, *Ceram. Int.* 37 (2011) 1705–1724.
- [36] J. Jeevaratnam, L.S.D. Glasser, F.P. Glasser, *Nature* 194 (1962) 764–765.
- [37] P.P. Evseev, A.F. Filippov, *Izv. Vysshikh Uchebnykh Zaved. Chernaya Metall.* 10 (1967) No. 3, 55–59.
- [38] M. Zielinski, B. Sikora, *Pr. Inst. Metal. Żelaza* 29 (1977) 229–232.
- [39] H. Kobatake, J. Brillo, *J. Mater. Sci.* 48 (2013) 4934–4941.
- [40] Z. Li, K. Mukai, M. Zeze, K.C. Mills, *J. Mater. Sci.* 40 (2005) 2191–2195.
- [41] J. Choe, H.G. Kim, Y. Jeon, H.J. Park, Y. Kang, S. Ozawa, J. Lee, *ISIJ Int.* 54 (2014) 2104–2108.
- [42] A. Milne, A. Amirfazli, *Adv. Colloid Interface Sci.* 170 (2012) 48–55.

- [43] W.Y. Kim, G.J. Nam, S.Y. Kim, *Metall. Mater. Trans. B* 52 (2021) 1508–1520.
- [44] H. Barati, M. Wu, A. Kharicha, A. Ludwig, *Powder Technol.* 329 (2018) 181–198.

Springer Nature or its licensor holds exclusive rights to this article under a publishing agreement with the author(s) or other rightsholder(s); author self-archiving of the accepted manuscript version of this article is solely governed by the terms of such publishing agreement and applicable law.